arXiv:2010.11765v2 [q-bio.NC] 8 Dec 2020

Identifying Learning Rules From Neural Network Observables

Aran Nayebi[1,*], **Sanjana Srivastava**[2,*], **Surya Ganguli**[3,5], **and Daniel L.K. Yamins**[2,4,5]

[1]Neurosciences Ph.D. Program, Stanford University
[2]Department of Computer Science, Stanford University
[3]Department of Applied Physics, Stanford University
[4]Department of Psychology, Stanford University
[5]Wu Tsai Neurosciences Institute, Stanford University
[*]Equal contribution. Correspondence: anayebi@stanford.edu

Abstract

The brain modifies its synaptic strengths during learning in order to better adapt to its environment. However, the underlying plasticity rules that govern learning are unknown. Many proposals have been suggested, including Hebbian mechanisms, explicit error backpropagation, and a variety of alternatives. It is an open question as to what specific experimental measurements would need to be made to determine whether any given learning rule is operative in a real biological system. In this work, we take a "virtual experimental" approach to this problem. Simulating idealized neuroscience experiments with artificial neural networks, we generate a large-scale dataset of learning trajectories of aggregate statistics measured in a variety of neural network architectures, loss functions, learning rule hyperparameters, and parameter initializations. We then take a discriminative approach, training linear and simple non-linear classifiers to identify learning rules from features based on these observables. We show that different classes of learning rules can be separated solely on the basis of aggregate statistics of the weights, activations, or instantaneous layer-wise activity changes, and that these results generalize to limited access to the trajectory and held-out architectures and learning curricula. We identify the statistics of each observable that are most relevant for rule identification, finding that statistics from network activities across training are more robust to unit undersampling and measurement noise than those obtained from the synaptic strengths. Our results suggest that activation patterns, available from electrophysiological recordings of post-synaptic activities on the order of several hundred units, frequently measured at wider intervals over the course of learning, may provide a good basis on which to identify learning rules.

1 Introduction

One of the tenets of modern neuroscience is that the brain modifies its synaptic connections during learning to improve behavior [Hebb, 1949]. However, the underlying plasticity rules that govern the process by which signals from the environment are transduced into synaptic updates are unknown. Many proposals have been suggested, ranging from Hebbian-style mechanisms that seem biologically plausible but have not been shown to solve challenging real-world learning tasks [Bartunov et al., 2018]; to backpropagation [Rumelhart et al., 1986], which is effective from a learning perspective but has numerous biologically implausible elements [Grossberg, 1987, Crick, 1989]; to recent regularized circuit mechanisms that succeed at large-scale learning while remedying some of the implausibilities of backpropagation [Akrout et al., 2019, Kunin et al., 2020].

34th Conference on Neural Information Processing Systems (NeurIPS 2020), Vancouver, Canada.

A major long-term goal of computational neuroscience will be to identify which of these routes is most supported by neuroscience data, or to convincingly identify experimental signatures that reject all of them and suggest new alternatives. However, along the route to this goal, it will be necessary to develop practically accessible experimental observables that can efficiently separate between hypothesized learning rules. In other words, what specific measurements – of activation patterns over time, or synaptic strengths, or paired-neuron input-output relations – would allow one to draw quantitatively tight estimates of whether the observations are more consistent with one or another specific learning rule? This in itself turns out to be a substantial problem, because it is difficult on purely theoretical grounds to identify which patterns of neural changes arise from given learning rules, without also knowing the overall network architecture and loss function target (if any) of the learning system.

In this work, we take a "virtual experimental" approach to this question, with the goal of answering whether it is even possible to generically identify which learning rule is operative in a system, across a wide range of possible learning rule types, system architectures, and loss targets; and if it is possible, which types of neural observables are most important in making such identifications. We simulate idealized neuroscience experiments with artificial neural networks trained using different learning rules, across a variety of architectures, tasks, and associated hyperparameters. We first demonstrate that the learning rules we consider can be reliably separated *without* knowledge of the architecture or loss function, solely on the basis of the trajectories of aggregate statistics of the weights, activations, or instantaneous changes of post-synaptic activity relative to pre-synaptic input, generalizing as well to unseen architectures and training curricula. We then inject realism into how these measurements are collected in several ways, both by allowing access to limited portions of the learning trajectory, as well as subsampling units with added measurement noise. Overall, we find that measurements temporally spaced further apart are more robust to trajectory undersampling. We find that aggregated statistics from recorded activities across training are most robust to unit undersampling and measurement noise, whereas measured weights (synaptic strengths) provide reliable separability as long as there is very little measurement noise but can otherwise be relatively susceptible to comparably small amounts of noise.

2 Related Work

Lim et al. [2015] infer a Hebbian-style plasticity rule from IT firing rates recorded in macaques to novel and familiar stimuli during a passive and an active viewing task. By assuming that the plasticity rule is a separable function of pre-synaptic and post-synaptic rates acting on a non-linear recurrent rate model, their result demonstrates that one can infer the *hyperparameters* of a learning rule from post-synaptic activities alone, given a specific architecture (e.g. recurrent excitatory to excitatory connections) and *single class* of learning rule (e.g. Hebbian).

Since Grossberg [1987] introduced the *weight transport problem*, namely that backpropagation requires exact transposes to propagate errors through the network, many credit assignment strategies have proposed circumventing the problem by introducing a distinct set of feedback weights to propagate the error backwards. Broadly speaking, these proposals fall into two groups: those that encourage symmetry between the forward and backward weights [Lillicrap et al., 2016, Nøkland, 2016, Liao et al., 2016, Xiao et al., 2019, Moskovitz et al., 2018, Akrout et al., 2019, Kunin et al., 2020], and those that encourage preservation of information between neighboring network layers [Bengio, 2014, Lee et al., 2015, Kunin et al., 2020].

However, Kunin et al. [2020] show that temporally-averaged post-synaptic activities from IT cortex (in adult macaques during passive viewing of images) are not sufficient to separate many different *classes* of learning rules, even for a fixed architecture. This suggests that neural data most useful for distinguishing between classes of learning rules in an *in vivo* neural circuit will likely require more temporally-precise measurements during learning, but does not prescribe what quantities should be measured.

In artificial networks, every unit can be measured precisely and the ground truth learning rule is known, which may provide insight as to what experimentally measurable observables may be most useful for inferring the underlying learning rule. In the case of single-layer linear perceptrons with Gaussian inputs, the error curves for a mean-squared error loss can be calculated exactly from the unit-averaged weight updates [Baldi and Hornik, 1989, Heskes and Kappen, 1991, Werfel et al.,

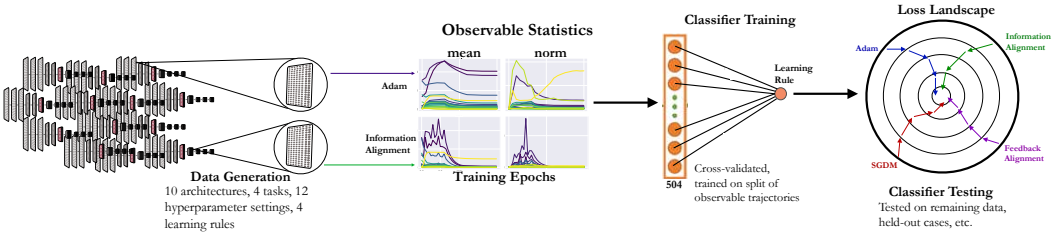

Figure 1: **Overall approach.** Observable statistics are generated from each layer of 1,056 neural networks, through the model training process for each learning rule. Qualitatively, trajectories show patterns that are common across the observable statistics and distinctive among learning rules. We take a quantitative approach whereby a classifier is cross-validated and trained on a subset of these trajectories and evaluated on the remaining data.

2004]. Of course, it is not certain whether this signal would be useful for multi-layered networks across multiple loss functions, architectures, and highly non-Gaussian inputs at scale.

In order to bear on future neuroscience experiments, it will be important to identify useful aggregate statistics (beyond just the mean) and how robust these observable statistics are when access to the full learning trajectory is no longer allowed, or if they are only computed from a subset of the units with some amount of measurement noise.

3 Approach

Defining features. The primary aim of this study is to determine the general separability of classes of learning rules. Fig. 1 indicates the general approach of doing so, and the first and second panels illustrate feature collection. In order to determine what needs to be measured to reliably separate classes of learning rules, we begin by defining representative features that can be drawn from the course of model training. For each layer in a model, we consider three measurements: **weights** of the layer, **activations** from the layer, and **layer-wise activity change** of a given layer's outputs relative to its inputs. We choose artificial neural network weights to analogize to synaptic strengths in the brain, activations to analogize to post-synaptic firing rates, and layer-wise activity changes to analogize to *paired* measurements that involve observing the change in post-synaptic activity with respect to changes induced by pre-synaptic input. The latter observable is motivated by experiments that result in LTP induction via tetanic stimulation [Wojtowicz and Atwood, 1985], in the limit of an infinitesimally small bin-width.

For each measure, we consider three functions applied to it: identity, absolute value, and square. Finally, for each function of the weights and activations, we consider seven statistics: Frobenius norm, mean, variance, skew, kurtosis, median, and third quartile. For the layer-wise activity change observable, we only use the mean statistic because instantaneous layer-wise activity change is operationalized as the gradient of outputs with respect to inputs (definable for *any* learning rule, regardless of whether or not it uses a gradient of an error signal to update the weights). The total derivative across neurons can be computed efficiently, but computing the derivative for every output neuron in a given layer is prohibitively computationally complex. This results in a total of 45 continuous valued observable statistics for each layer, though 24 observable statistics (listed in Fig. 3) are ultimately used for training the classifiers, since we remove any statistic that has a divergent value during the course of model training. We also use a ternary indicator of **layer position** in the model hierarchy: "early", "middle", or "deep" (represented as a one-hot categorical variable).

Constructing a varied dataset. We use the elements of a trained model other than learning rule as factors of variation. Specifically, we vary architectures, tasks, and learning hyperparameters. The tasks and architectures we consider are those that have been shown to produce good representations to (mostly primate) sensory neural and behavioral data [Yamins et al., 2014, Kell et al., 2018, Nayebi et al., 2018, Schrimpf et al., 2018, Cadena et al., 2019, Feather et al., 2019]. Specifically, we consider the tasks of **supervised 1000-way ImageNet categorization** [Deng et al., 2009], ***self-supervised* ImageNet** in the form of the recent competitively performing "SimCLR" contrastive loss

and associated data augmentations [Chen et al., 2020], **supervised 794-way Word-Speaker-Noise (WSN) categorization** [Feather et al., 2019], and **supervised ten-way CIFAR-10 categorization** [Krizhevsky, 2010]. We consider six architectures on ImageNet, SimCLR, and WSN, namely, ResNet-18, ResNet-18v2, ResNet-34, and ResNet-34v2 [He et al., 2016], as well as Alexnet [Krizhevsky et al., 2012] both without and with local response normalization (denoted as Alexnet-LRN). On CIFAR-10, we consider four shallower networks consisting of either 4 layers with local response normalization, due to Krizhevsky [Krizhevsky, 2012], or a 5 layer variant (denoted as KNet4-LRN and KNet5-LRN, respectively), as well as without it (denoted as KNet4 and KNet5). The latter consideration of these networks on CIFAR-10 is perhaps biologically interpretable as expanding scope to shallower *non-primate* (e.g. mouse) visual systems [Harris et al., 2019].

The dependent variable is the learning rule (across hyperparameters), and we consider four: **stochastic gradient descent with momentum (SGDM)** [Sutskever et al., 2013], **Adam** [Kingma and Ba, 2014], **feedback alignment (FA)** [Lillicrap et al., 2016], and **information alignment (IA)** [Kunin et al., 2020]. Learning hyperparameters for each model under a given learning rule category are the Cartesian product of three settings of batch size (128, 256, and 512), two settings of the random seed for architecture initialization (referred to as "model seed"), and two settings of the random seed for dataset order (referred to as "dataset randomization seed"). The base learning rate is allowed to vary depending on what is optimal for a given architecture on a particular dataset and is rescaled accordingly for each batch size setting. All model training details can be found in Appendix A.

We select these learning rules as they span the space of commonly used variants of backpropagation (SGDM and Adam), as well as potentially more biologically-plausible "local" learning rules that efficiently train networks at scale to varying degrees of performance (FA and IA) and avoid weight transport. We do not explicitly train models with more classic learning rules such as pure Hebbian learning or weight/node perturbation [Widrow and Lehr, 1990, Jabri and Flower, 1992], since for the multi-layer non-linear networks that we consider here, those learning rules are either highly inefficient in terms of convergence (e.g. weight/node perturbation [Werfel et al., 2004]) or they will readily fail to train due to a lack of stabilizing mechanism (e.g. pure Hebbian learning). However, the local learning rules rules we do consider (FA and IA) incorporate salient aspects of these algorithms in their implementation – IA incorporates Hebbian and other stabilizing mechanisms in its updates to the feedback weights and FA employs a pseudogradient composed of random weights reminiscent of weight/node perturbation.

To gain insight into the types of observables that separate learning rules in general, we use statistics (averaged across the validation set) generated from networks trained across 1,056 experiments as a feature set on which to train simple classifiers, such as a linear classifier (SVM) and non-linear classifiers (Random Forest and a Conv1D MLP) on various train/test splits of the data. This is illustrated in the third and fourth panels of Fig. 1, with the feature and parameter selection procedure detailed in Appendices B.1 and B.2.

4 Results on Full Dataset

In this section, we examine learning rule separability when we have access to the entire training trajectories of the models, as well as noiseless access to *all* units. This will allow us to assess whether the learning rules can be separated independent of loss function and architecture, what types of observables and their statistics are most salient for separability, and how robust these conclusions are to certain classes of input types to explore strong generalization.

General separability problem is tractable. For each observable measure, we train the classifier on the concatenation of the trajectory of statistics identified in §3, generated from each model layer. Already by eye (Fig. 1), one can pick up distinctive differences across the learning rules for each of the training trajectories of these metrics. Of course, this is not systematic enough to clearly judge one set of observables versus another, but provides some initial assurance that these metrics seem to capture some inherent differences in learning dynamics across rules.

As can be seen from Fig. 2(a), across all classes of observables, the Random Forest attains the highest test accuracy, and all observable measures perform similarly under this classifier, even when distinguishing between any given pair of learning rules (Fig. S1). The Conv1D MLP never outperforms the Random Forest, and only slightly outperforms the SVM in most cases, despite having the capability of learning additional non-linear features beyond the input feature set.

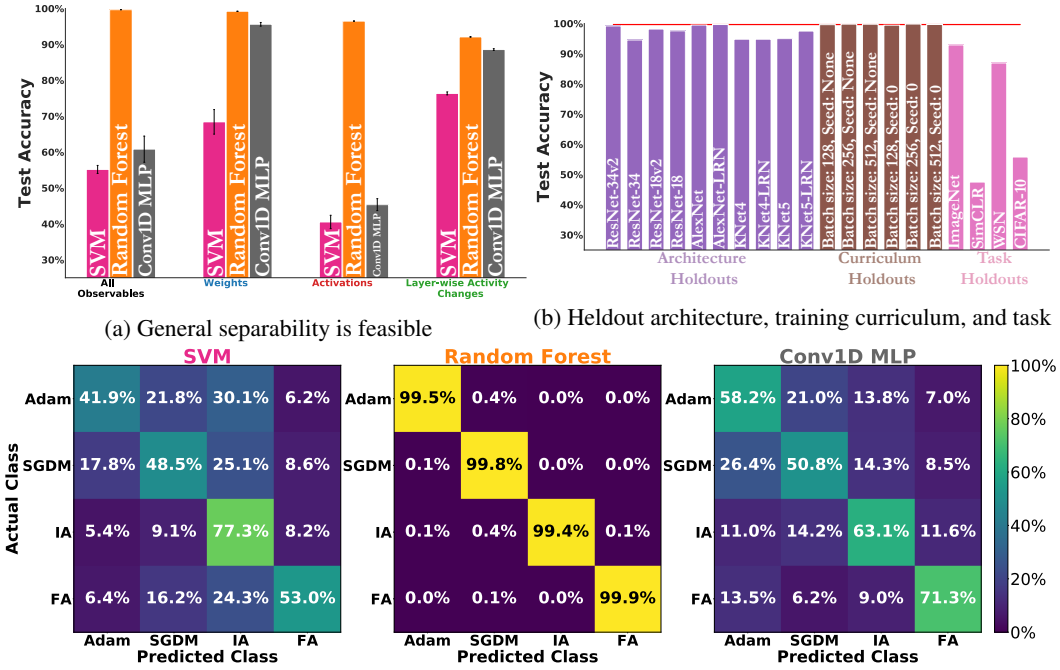

(a) General separability is feasible

(b) Heldout architecture, training curriculum, and task

(c) Differences in learning rate policy (Adam vs. SGDM) are more difficult to distinguish

Figure 2: **Quantifying successful separation.** **(a)** shows the test accuracy of each classifier, with mean and s.e.m. across ten category-balanced 75%/25% train/test splits, using the observable measures in §3. **(b)** Let the red line indicate the mean and s.e.m. test accuracy of the Random Forest trained on all observable measures in (a). The left-most violet bars indicate Random Forest performance when holding out *all* examples from each of the ten architectures we consider, for each observable measure. The middle brown bars indicate Random Forest performance when holding out *all* examples from each of the six combinations of batch size and dataset randomization seed pair. The right-most pink bars indicate Random Forest performance when holding out *all* examples from each of the four tasks. **(c)** Confusion matrices on the test set (1,296 examples per class), averaged across the ten category-balanced 75%/25% train/test splits, for each of the three classifiers when trained on all observable measures in (a). Chance performance in these settings is 25% test accuracy.

In fact, from the confusion matrices in Fig. 2(c), the Random Forest hardly mistakes one learning rule from any of the others. However, when the classifiers make mistakes, they tend to confuse Adam vs. SGDM more so than IA vs. FA, suggesting that they are able to pick up more on differences, reflected in the observable statistics, due to high-dimensional direction of the gradient tensor than the magnitude of the gradient tensor (the latter directly tied to learning rate policy).

In terms of linear separability, the SVM can attain its highest test accuracy using either the weight or layer-wise activity change observables. Interestingly, the layer-wise activity change observable has the least number of statistics (three) associated with it compared to the weight and activation observables. The class of learning rule, however, is least able to be *linearly* determined from the activation observables. The latter observation holds as well when distinguishing between any given pair of learning rules (Fig. S1).

To further gain insight into drivers of learning rule discriminability, we consider two additional sets of controls, namely that of task performance and the scale of observable statistics. In Fig. S2(a), we find that where defined, task performance is a confounded indicator of separability. SGDM and IA are easily separated by classifiers trained on any observable measure, despite yielding similar top-1 validation accuracy on ImageNet across ResNet architectures and hyperparameters.

In Fig. S2(b), we train classifiers on observable statistics averaged over the whole learning trajectory. We find that averaging the trajectory hurts performance, relative to having the full trajectory, for the (linear) SVM classifier across all classes of observables. This is also the case for the Random Forest, but far less for the weight observable statistics, suggesting this type of non-linear classifier

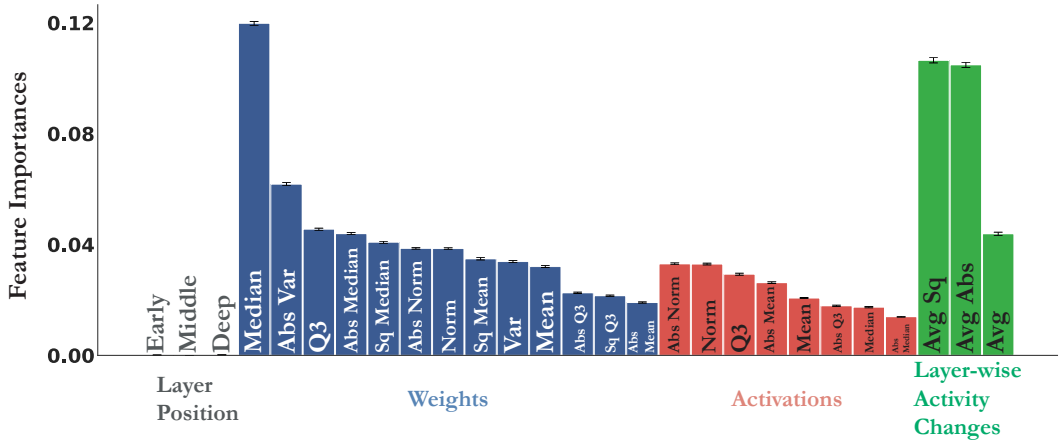

Figure 3: **Relative importances of observable statistics.** We show the Gini impurity feature importance (summed across the learning trajectory) of each observable statistic for the Random Forest classifier trained on all observable measures in Fig. 2(a). The colors indicate observable measures, demonstrating the prevalence and importance of observable statistics from a given measure. Mean and s.e.m. across trees in the Random Forest and ten category-balanced 75%/25% train/test splits. "Sq" and "Abs" indicate squaring or taking the absolute value across all units prior to computing the statistic, respectively. "Q3" is the abbreviation for the third quartile statistic.

has enough information from the trajectory-averaged weight statistics during the course of learning to decode the identity of the learning rule. Overall, this result suggests that the scale of the observable statistics is not sufficient in all cases to distinguish learning rules, though it certainly contributes in part to it.

Generalization to entire held-out classes of input types. The results so far were obtained across ten category-balanced splits of examples with varying tasks, model architectures, and training curricula. However, it is not clear from the above whether our approach will generalize to *unseen* architectures and training curricula. In particular, if a new "animal" were added to our study, we ideally do not want to be in a position to have to completely retrain the classifier or have the conclusions change drastically, nor do we want the conclusions to be highly sensitive to training curricula (the latter analogized in this case to batch size and dataset randomization seed).

As seen in Fig. 2(b), the performance of the Random Forest for the held out conditions of architecture and training curriculum is not much worse than its corresponding test set performance in Fig. 2(a), indicated by the red line. This relative robustness across architectures and training curricula holds even if you train on either the weight or activation observable measures individually (Fig. S3(a,b)), but not as consistently with the layer-wise activity changes (Fig. S3(a)) or with a linear classifier (Fig. S4(a,b)).

We also tested held-out task to quantify differences in learning dynamics between different tasks, although it is not necessarily reflective of a real experimental condition where task is typically fixed. In particular, generalizing to deep models trained on ImageNet or WSN works the best, despite them being different sensory modalities. However, generalizing from the supervised cross-entropy loss to the self-supervised SimCLR loss performs the lowest, as well as generalizing from deep architectures on ImageNet, SimCLR, and WSN to shallow architectures on CIFAR-10 (in the latter case, both task and architecture have changed from the classifier's train to test set). This quantifies potentially fundamental differences in learning dynamics between supervised vs. self-supervised tasks and between deep networks on large-scale tasks vs. shallow networks on small-scale tasks.

Taken together, Fig. 2 suggests that a simple non-linear classifier (Random Forest) can attain consistently high generalization performance when trained across a variety of tasks with either the weight or activation observable measures *alone*.

Aggregate statistics are not equally important. We find from the Random Forest Gini impurity feature importances for each measure's individual statistic that not all the aggregate statistics within a given observable measure appear to be equally important for separating learning rules, as displayed

in Fig. 3. For the weights, the median is given the most importance, even in an absolute sense across all other observable measures. For the activations, the norm statistics are given the most importance for that measure. For the averaged (across output units) layer-wise activity changes, the magnitude of this statistic either in terms of absolute value or square are assigned similar importances. On the other hand, the first three features comprising the ternary categorical "layer position" are assigned the lowest importance values.

Of course, we do not want to over-interpret these importance values given that Gini impurity has a tendency to bias continuous or high cardinality features. The more computationally expensive permutation feature importance could be less susceptible to such bias. However, these results are suggestive that for a given observable measure, there may only be a small subset of statistics most useful for learning rule separability, indicating that in a real experiment, it might not be necessary to compute very many aggregate statistics from recorded units so long as a couple of the appropriate ones for that measure (e.g. those identified from classifiers) are used. While no theory of neural networks yet allows us to derive optimal statistics mathematically (motivating our empirical approach), ideally in the future we can combine better theory with our method to sharpen feature design.

5 Access to Only Portions of the Learning Trajectory

The results in §4 were obtained with access to the entire learning trajectory of each model. Often however, an experimentalist collects data throughout learning at regularly spaced intervals [Holtmaat et al., 2005]. We capture this variability by randomly sampling a fixed number of samples at a fixed spacing ("subsample period") from each trajectory, as is done in Fig. 4(a). See Appendix B.3.1 for additional details on the procedure.

We find across observable measures that robustness to undersampling of the trajectory is largely dependent on the subsample period length (number of epochs between consecutive samples). As the subsample period length increases (middle and right-most columns of Fig. 4(a)), the Random Forest classification performance[1] increases compared to the *same* number of samples for a smaller period (left-most column).

To further demonstrate the importance of subsampling widely *across* the learning trajectory, we train solely on a consecutive third of the trajectory ("early", "middle", or "late") and separately test on each of the remaining consecutive thirds in Fig. 4(b). This causes a reduction in generalization performance relative to training and testing on the *same* consecutive portion (though there is some correspondence between the middle and late portions). For a fixed observable measure, even training and testing on the same consecutive portion of the learning trajectory does not give consistent performance across portions (Fig. S6). The use of a non-linear classifier is especially crucial in this setting, as the (linear) SVM often attains chance test accuracy or close to it (Fig. S7).

Taken together, these results suggest that data that consists of measurements collected temporally further apart across the learning trajectory is more robust to undersampling than data collected closer together in training time. Furthermore, across *individual* observable measures, the *weights* are overall the most robust to undersampling of the trajectory, but with enough frequency of samples we can achieve comparable performance with the activations.

6 Unit Undersampling and Measurement Noise Robustness of Observables

The aggregate statistics computed from the observable measures have thus far operated under the idealistic assumption of noiseless access to every unit in the model. However, in most datasets, there is a significant amount of unit undersampling as well as non-zero measurement noise. How do these two factors affect learning rule identification, and in particular, how noise and subsample-robust are particular observable measures? Addressing this question would provide insight into the types of experimental paradigms that may be most useful for identifying learning rules, and predict how certain experimental tools may fall short for given observables.

To assess this question, we consider an anatomically reasonable feedforward model of primate visual cortex, ResNet-18, trained on both supervised ImageNet and the self-supervised SimCLR

[1] The advantage of larger subsample period lengths holds for a linear classifier such as the SVM (Fig. S5), but as expected, absolute performance is lower.

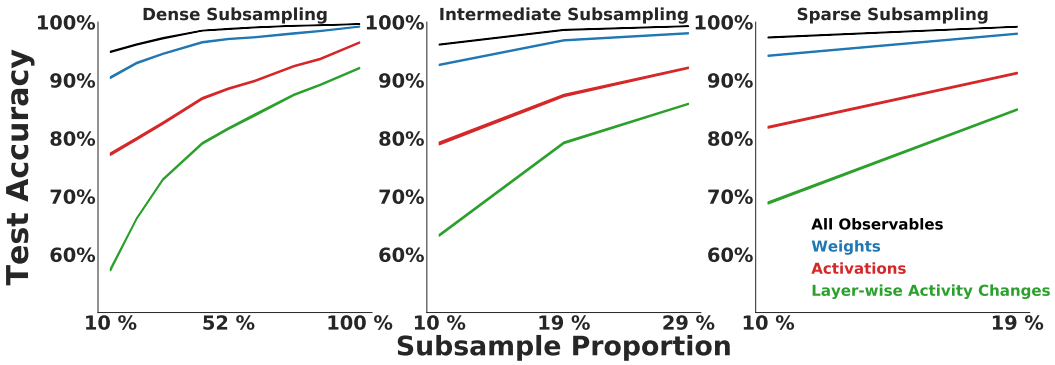

(a) Sparse subsampling *across* the learning trajectory is robust to trajectory undersampling.

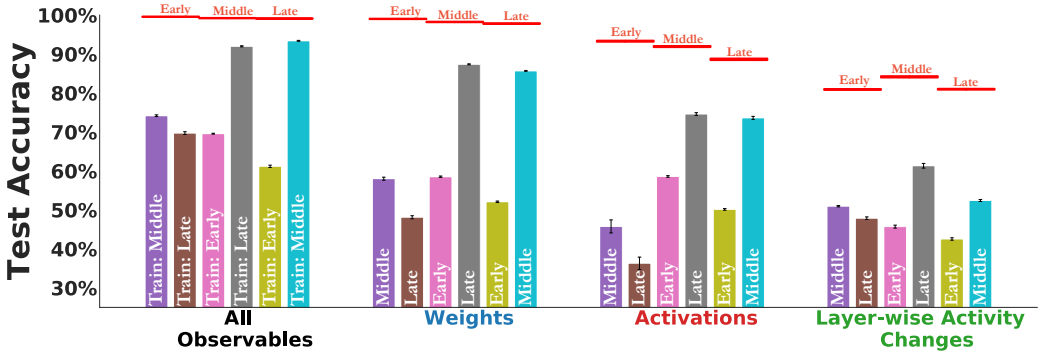

(b) Training solely on consecutive portions of the learning trajectory is *not* robust to trajectory undersampling.

Figure 4: **Trajectory subsampling.** **(a)** Sparse subsampling, where the epochs between nearby trajectory samples are the furthest apart (right panel; 25 epochs apart), requires far fewer samples to achieve the same performance for the Random Forest as the full trajectory (left panel; 5 epochs apart). "Subsample Proportion $Y\%$" refers to the number of samples chosen for the trajectory subsample relative to that of the full trajectory (21 total samples). **(b)** We train the Random Forest on 75% of examples with access to only one consecutive third of the full trajectory (7 consecutive samples each out of 21 total samples), testing on the remaining 25% of examples from one of the other two consecutive thirds. Red lines denote Random Forest performance when tested on 25% of examples from the *same* portion of the trajectory as in classifier training for each observable measure, reported in the bottom right row of Fig. S6. Mean and s.e.m. in all cases are across ten category-balanced train/test splits. Chance performance in these settings is 25% test accuracy.

tasks (known to give neurally-plausible representations [Nayebi et al., 2018, Schrimpf et al., 2018, Zhuang et al., 2020]). We train the network with FA and IA, for which there have been suggested biologically-motivated mechanisms [Guerguiev et al., 2017, Lansdell and Kording, 2019, Kunin et al., 2020].

We model measurement noise as a standard additive white Gaussian noise (AWGN) process applied independently per unit with five values of standard deviation (including the case of no measurement noise). We subsample units from a range that is currently used by electrophysiological techniques[2] up to the case of measuring all of the units. See Appendix B.4 for additional details on the procedure.

From Fig. 5, we find that both the weight and layer-wise activity change observables are the most susceptible to unit undersampling and noise in measurements. The activations observable is the most robust across all noise and unit subsampling levels (regardless of classifier, see Fig. S8 for the SVM).

This data suggests that if one collects experimental data by imaging synaptic strengths, it is still crucial that the optical imaging readout not be very noisy, since even with the amount of units

[2]Based on estimates of the total neuronal density in visual cortex being on the order of hundreds of millions [DiCarlo et al., 2012], compared to the number of units typically recorded on the order of several hundred [Majaj et al., 2015, Kar et al., 2019].

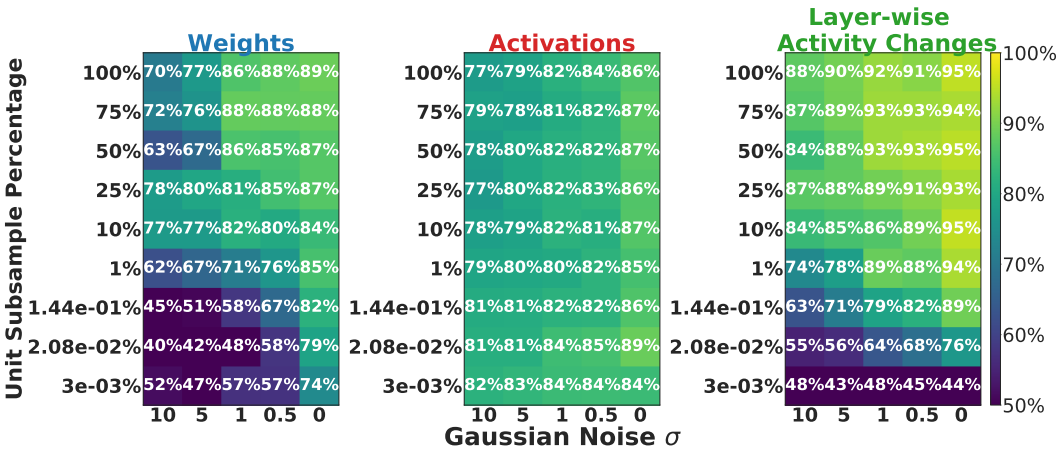

Figure 5: **Activations are the most robust to measurement noise and unit undersampling.** For each observable measure, the Random Forest test accuracy separating FA vs. IA on ResNet-18 across the ImageNet and SimCLR tasks, averaged across random seed and ten category-balanced 75%/25% train/test splits. The x-axis from the left to right of each heatmap corresponds to decreasing levels of noise, and the y-axis from bottom to top corresponds to increasing levels of sampled units. Top right corner of each heatmap corresponds to the perfect information setting of §4. Chance performance in this setting is 50% test accuracy.

typically recorded currently (e.g. several hundred to several thousand synapses, $\sim 2.08 \times 10^{-2}\%$ or less), a noisy imaging strategy of synaptic strengths may be rendered ineffective. Instead, current electrophysiological techniques that measure the *activities* from hundreds of units ($\sim 3 \times 10^{-3}\%$) could form a good set of neural data to separate learning rules. Recording more units with these techniques can improve learning rule separability from the activities, but it does not seem necessary, at least in this setting, to record a *majority* of units to perform this separation effectively.

7 Discussion

In this work, we undertake a "virtual experimental" approach to the problem of identifying measurable observables that may be most salient for separating hypotheses about synaptic updates in the brain. We have made this dataset publicly available[3], enabling others to analyze properties of learning rules without needing to train neural networks.

Through training 1,056 neural networks at scale on both supervised and self-supervised tasks, we find that across architectures and loss functions, it is possible to reliably identify what learning rule is operating in the system only on the basis of aggregate statistics of the weights, activations, or layer-wise activity changes. We find that with a simple non-linear classifier (Random Forest), each observable measure forms a relatively comparable feature set for predicting the learning rule category.

We next introduced experimental realism into how these observable statistics are measured, either by limiting access to the learning trajectory or by subsampling units with added noise. We find that measurements temporally spaced further apart are more robust to trajectory undersampling across all observable measures, especially compared to those taken at consecutive portions of the trajectory. Moreover, aggregate statistics across units of the network's activation patterns are most robust to unit undersampling and measurement noise, unlike those obtained from the synaptic strengths alone.

Taken together, our findings suggest that *in vivo* electrophysiological recordings of post-synaptic activities from a neural circuit on the order of several hundred units, frequently measured at wider intervals during the course of learning, may provide a good basis on which to identify learning rules. This approach provides a computational footing upon which future experimental data can be used to identify the underlying plasticity rules that govern learning in the brain.

[3] `https://github.com/neuroailab/lr-identify`

Broader Impact

Our work provides a basis as to what neuroscience experimental data should be collected in order to infer plasticity rules. Therefore, the experimental neuroscience community may benefit from this research. The data in this research is collected from neural networks trained on the ImageNet, Word-Speaker-Noise (WSN), and CIFAR-10 datasets. There is well-documented evidence of bias emerging from deep neural networks trained on field-standard large-scale image databases, with many ethical harms stemming from use of the biased algorithms to make important decisions on social policy or limit civil liberties. Rather than using network classifications in a real-world context, our study uses observable measurements from within the network mechanism as simulated brain data. This data is not interpretable to humans and is ultimately used to train and test a classifier to separate learning rules, which are a mathematical formulation and agnostic to any community. This study therefore does not leverage any bias in the data. However, identifying neural network observables that distinguish learning rules presents obvious privacy concerns which could be exploited, for example, to generate adversarial attacks or even to recover training data. It is possible that the observable statistics reflect the workings of a biased "*in silico* brain", in which case the classifier used to separate learning rules may be biased in that it has only been trained and tested on networks whose training data may be biased differently than the training data animals typically receive. This is a problem not just for this study, but generally comes down to available network-training tasks, especially those of the scale needed to provide neurally-plausible representations. Tasks are the most computationally complex factor of variation to add values to, so diversifying the set of tasks is an ongoing effort, and we hope to use balanced, ethically verified large-scale datasets as they become available. Furthermore, given the limited number of subjects in neuroscience experiments, this type of bias is not new in our experiment; the scalability of our approach may provide a way to have more representative data. The only consequence of failure is that the experiment which is performed on the basis of the conclusions we draw may not be as decisive in determining the learning rule.

Acknowledgments and Disclosure of Funding

We thank Katherine L. Hermann, Eshed Margalit, and Jinyao Yan for helpful discussions. We thank the anonymous reviewers for their comments and suggestions. This work was funded in part by the IBM-Watson AI Lab. S.S. is supported by the National Science Foundation Graduate Research Fellowship Program (NSF GRFP). S.G. is supported by the James S. McDonnell Foundation, Simons Foundation, and National Science Foundation CAREER Award. D.L.K.Y is supported by the James S. McDonnell Foundation (Understanding Human Cognition Award Grant No. 220020469), the Simons Foundation (Collaboration on the Global Brain Grant No. 543061), the Sloan Foundation (Fellowship FG-2018-10963), the National Science Foundation (RI 1703161 and CAREER Award 1844724), the DARPA Machine Common Sense program, and hardware donation from the NVIDIA Corporation. We thank the Google TensorFlow Research Cloud (TFRC) team for generously providing TPU hardware resources for this project.

References

M. Akrout, C. Wilson, P. Humphreys, T. Lillicrap, and D. B. Tweed. Deep learning without weight transport. In *Advances in Neural Information Processing Systems*, pages 974–982, 2019.

P. Baldi and K. Hornik. Neural networks and principal component analysis: Learning from examples without local minima. *Neural networks*, 2(1):53–58, 1989.

S. Bartunov, A. Santoro, B. Richards, L. Marris, G. E. Hinton, and T. Lillicrap. Assessing the scalability of biologically-motivated deep learning algorithms and architectures. In *Advances in Neural Information Processing Systems*, pages 9368–9378, 2018.

Y. Bengio. How auto-encoders could provide credit assignment in deep networks via target propagation. *ArXiv*, abs/1407.7906, 2014.

P. Buchlovsky, D. Budden, D. Grewe, C. Jones, J. Aslanides, F. Besse, A. Brock, A. Clark, S. G. Colmenarejo, A. Pope, et al. Tf-replicator: Distributed machine learning for researchers. *arXiv preprint arXiv:1902.00465*, 2019.

S. A. Cadena, G. H. Denfield, E. Y. Walker, L. A. Gatys, A. S. Tolias, M. Bethge, and A. S. Ecker. Deep convolutional models improve predictions of macaque v1 responses to natural images. *PLoS computational biology*, 15(4):e1006897, 2019.

T. Chen, S. Kornblith, M. Norouzi, and G. Hinton. A simple framework for contrastive learning of visual representations. In *The 37th International Conference on Machine Learning (ICML 2020)*, 2020. URL `https://arxiv.org/abs/2002.05709`.

F. Crick. The recent excitement about neural networks. *Nature*, 337:129–132, 1989. doi: 10.1038/337129a0.

J. Deng, W. Dong, R. Socher, L.-J. Li, K. Li, and L. Fei-Fei. Imagenet: A large-scale hierarchical image database. In *2009 IEEE conference on computer vision and pattern recognition*, pages 248–255. Ieee, 2009.

J. J. DiCarlo, D. Zoccolan, and N. C. Rust. How does the brain solve visual object recognition? *Neuron*, 73(3): 415–434, 2012.

J. Feather, A. Durango, R. Gonzalez, and J. McDermott. Metamers of neural networks reveal divergence from human perceptual systems. In *Advances in Neural Information Processing Systems*, pages 10078–10089, 2019.

J. F. Gemmeke, D. P. Ellis, D. Freedman, A. Jansen, W. Lawrence, R. C. Moore, M. Plakal, and M. Ritter. Audio set: An ontology and human-labeled dataset for audio events. In *2017 IEEE International Conference on Acoustics, Speech and Signal Processing (ICASSP)*, pages 776–780. IEEE, 2017.

S. Grossberg. Competitive learning: From interactive activation to adaptive resonance. *Cognitive Science*, 11: 23–63, 1987.

J. Guerguiev, T. P. Lillicrap, and B. A. Richards. Towards deep learning with segregated dendrites. *eLife*, 6, 2017. doi: 10.7554/eLife.22901.

J. A. Harris, S. Mihalas, K. E. Hirokawa, J. D. Whitesell, H. Choi, A. Bernard, P. Bohn, S. Caldejon, L. Casal, A. Cho, et al. Hierarchical organization of cortical and thalamic connectivity. *Nature*, 575(7781):195–202, 2019.

K. He, X. Zhang, S. Ren, and J. Sun. Deep Residual Learning for Image Recognition. In *2016 IEEE Conference on Computer Vision and Pattern Recognition (CVPR)*, pages 770–778, June 2016. doi: 10.1109/CVPR.2016.90. ISSN: 1063-6919.

D. O. Hebb. *The organization of behavior: a neuropsychological theory*. J. Wiley; Chapman & Hall, 1949.

T. M. Heskes and B. Kappen. Learning processes in neural networks. *Physical Review A*, 44(4):2718, 1991.

A. J. Holtmaat, J. T. Trachtenberg, L. Wilbrecht, G. M. Shepherd, X. Zhang, G. W. Knott, and K. Svoboda. Transient and persistent dendritic spines in the neocortex in vivo. *Neuron*, 45(2):279–291, 2005.

S. Ioffe and C. Szegedy. Batch normalization: Accelerating deep network training by reducing internal covariate shift. *arXiv preprint arXiv:1502.03167*, 2015.

M. Jabri and B. Flower. Weight perturbation: An optimal architecture and learning technique for analog vlsi feedforward and recurrent multilayer networks. *IEEE Transactions on Neural Networks*, 3(1):154–157, 1992.

K. Kar, J. Kubilius, K. Schmidt, E. B. Issa, and J. J. DiCarlo. Evidence that recurrent circuits are critical to the ventral stream's execution of core object recognition behavior. *Nature neuroscience*, 22(6):974–983, 2019.

A. J. Kell, D. L. Yamins, E. N. Shook, S. V. Norman-Haignere, and J. H. McDermott. A task-optimized neural network replicates human auditory behavior, predicts brain responses, and reveals a cortical processing hierarchy. *Neuron*, 98(3):630–644, 2018.

D. P. Kingma and J. Ba. Adam: A method for stochastic optimization. *arXiv preprint arXiv:1412.6980*, 2014.

A. Köhn, F. Stegen, and T. Baumann. Mining the spoken wikipedia for speech data and beyond. In *Proceedings of the Tenth International Conference on Language Resources and Evaluation (LREC'16)*, pages 4644–4647, 2016.

A. Krizhevsky. Cifar-10 and cifar-100 datasets. 2010. URL `https://www.cs.toronto.edu/~kriz/cifar.html`.

A. Krizhevsky. Cuda-convnet, 2012. URL `https://github.com/BVLC/caffe/blob/master/examples/cifar10/cifar10_full.prototxt`.

A. Krizhevsky, I. Sutskever, and G. E. Hinton. Imagenet classification with deep convolutional neural networks. In *Advances in neural information processing systems*, pages 1097–1105, 2012.

D. Kunin, A. Nayebi, J. Sagastuy-Brena, S. Ganguli, J. Bloom, and D. L. Yamins. Two routes to scalable credit assignment without weight symmetry. In *The 37th International Conference on Machine Learning (ICML 2020)*, 2020. URL https://arxiv.org/abs/2003.01513.

B. J. Lansdell and K. P. Kording. Spiking allows neurons to estimate their causal effect. *bioRxiv*, page 253351, 2019.

D.-H. Lee, S. Zhang, A. Fischer, and Y. Bengio. Difference target propagation. In *Joint european conference on machine learning and knowledge discovery in databases*, pages 498–515. Springer, 2015.

Q. Liao, J. Z. Leibo, and T. Poggio. How important is weight symmetry in backpropagation? In *Proceedings of the Thirtieth AAAI Conference on Artificial Intelligence*, AAAI'16, pages 1837–1844. AAAI Press, 2016. URL http://dl.acm.org/citation.cfm?id=3016100.3016156.

T. P. Lillicrap, D. Cownden, D. B. Tweed, and C. J. Akerman. Random synaptic feedback weights support error backpropagation for deep learning. *Nature Communications*, 7:13276, Nov. 2016. ISSN 2041-1723. doi: 10.1038/ncomms13276. URL https://www.nature.com/articles/ncomms13276.

S. Lim, J. L. McKee, L. Woloszyn, Y. Amit, D. J. Freedman, D. L. Sheinberg, and N. Brunel. Inferring learning rules from distributions of firing rates in cortical neurons. *Nature neuroscience*, 18(12):1804, 2015.

N. J. Majaj, H. Hong, E. A. Solomon, and J. J. DiCarlo. Simple learned weighted sums of inferior temporal neuronal firing rates accurately predict human core object recognition performance. *The Journal of neuroscience : the official journal of the Society for Neuroscience*, 35:13402–18, 2015 Sep 30 2015. ISSN 1529-2401. doi: 10.1523/JNEUROSCI.5181-14.2015.

T. H. Moskovitz, A. Litwin-Kumar, and L. F. Abbott. Feedback alignment in deep convolutional networks. *CoRR*, abs/1812.06488, 2018. URL http://arxiv.org/abs/1812.06488.

A. Nayebi, D. Bear, J. Kubilius, K. Kar, S. Ganguli, D. Sussillo, J. J. DiCarlo, and D. L. Yamins. Task-driven convolutional recurrent models of the visual system. In *Advances in Neural Information Processing Systems*, pages 5290–5301, 2018.

A. Nøkland. Direct feedback alignment provides learning in deep neural networks. 09 2016.

D. B. Paul and J. Baker. The design for the wall street journal-based csr corpus. In *Speech and Natural Language: Proceedings of a Workshop Held at Harriman, New York, February 23-26, 1992*, 1992.

D. E. Rumelhart, G. E. Hinton, and R. J. Williams. Learning representations by back-propagating errors. *Nature*, 323:533–536, October 1986. doi: 10.1038/323533a0.

M. Schrimpf, J. Kubilius, H. Hong, N. J. Majaj, R. Rajalingham, E. B. Issa, K. Kar, P. Bashivan, J. Prescott-Roy, K. Schmidt, et al. Brain-score: Which artificial neural network for object recognition is most brain-like? *BioRxiv*, page 407007, 2018.

I. Sutskever, J. Martens, G. Dahl, and G. Hinton. On the importance of initialization and momentum in deep learning. In *International conference on machine learning*, pages 1139–1147, 2013.

J. Werfel, X. Xie, and H. S. Seung. Learning curves for stochastic gradient descent in linear feedforward networks. In *Advances in neural information processing systems*, pages 1197–1204, 2004.

B. Widrow and M. A. Lehr. 30 years of adaptive neural networks: perceptron, madaline, and backpropagation. *Proceedings of the IEEE*, 78(9):1415–1442, 1990.

J. Wojtowicz and H. Atwood. Correlation of presynaptic and postsynaptic events during establishment of long-term facilitation at crayfish neuromuscular junction. *Journal of neurophysiology*, 54(2):220–230, 1985.

W. Xiao, H. Chen, Q. Liao, and T. Poggio. Biologically-plausible learning algorithms can scale to large datasets. In *International Conference on Learning Representations*, 2019. URL https://openreview.net/forum?id=SygvZ209F7.

D. L. Yamins, H. Hong, C. F. Cadieu, E. A. Solomon, D. Seibert, and J. J. DiCarlo. Performance-optimized hierarchical models predict neural responses in higher visual cortex. *Proceedings of the National Academy of Sciences*, 111(23):8619–8624, 2014.

Y. You, I. Gitman, and B. Ginsburg. Large batch training of convolutional networks. *arXiv preprint arXiv:1708.03888*, 2017.

C. Zhuang, S. Yan, A. Nayebi, M. Schrimpf, M. Frank, J. DiCarlo, and D. Yamins. Unsupervised neural network models of the ventral visual stream. *bioRxiv*, 2020.

A Model Training Details

We use TensorFlow version 1.13.1 to conduct all model training experiments. All model function code can be found here: `https://github.com/neuroailab/lr-identify/tree/main/tensorflow/Models`. The names of the model layers from which we generate observable statistics can be found here: `https://github.com/neuroailab/lr-identify/blob/main/tensorflow/Models/model_layer_names.py`.

The v2 variants of ResNets use the pre-activation of the weight layers rather than the post-activation used in the original versions [He et al., 2016]. Furthermore, the v2 variants of ResNets apply batch normalization [Ioffe and Szegedy, 2015] and ReLU to the input *prior* to the convolution, whereas the original variants apply these operations after the convolution. We use the TF Slim architectures for these two variants provided here: `https://github.com/tensorflow/models/tree/master/research/slim`.

Following Kunin et al. [2020], we replace tied weights in backpropagation with a regularization loss on untied forward and backward weights in order to train the alternative learning rules of FA [Lillicrap et al., 2016] and IA [Kunin et al., 2020] at scale. Each model layer consists of forward weights that parametrize the task objective function and the backward weights specify a descent direction, as implemented here: `https://github.com/neuroailab/neural-alignment`. The total network loss is defined as the sum of the task objective function $\mathcal{J}$ and the local alignment regularization $\mathcal{R}$. Setting $\mathcal{R} \equiv 0$ results in FA, and we use the same $\mathcal{R}$ and corresponding metaparameters for IA that were specified in Kunin et al. [2020]. SGDM refers to stochastic gradient descent with Nesterov momentum of 0.9 in all cases.

A.1 ImageNet

This dataset [Deng et al., 2009] consists of 1,218,167 training images and 50,000 validation images from 1,000 total categories. The architectures trained on this task are AlexNet, AlexNet-LRN, ResNet-18, ResNet-18v2, ResNet-34, and ResNet-34v2. All models, except for the v2 ResNets, are trained on the standard ResNet preprocessing with $224 \times 224 \times 3$ sized ImageNet images. As used in the TF Slim repository linked above, the v2 ResNets are trained with Inception preprocessing, which uses larger $299 \times 299 \times 3$ sized images. The ResNets used an L2 regularization of 1×10^{-4} and the AlexNets used an L2 regularization of 5×10^{-4}.

The base learning rate for SGDM and IA for the ResNet models is set to 0.125 for a batch size of 256, and linearly rescaled for the remaining batch sizes of 128 and 512. For AlexNet and AlexNet-LRN, this base learning rate is set an order of magnitude lower to 0.0125 since it does not employ batch normalization layers. For FA and Adam across all models, this base learning rate is 0.001 (in the case of FA, the Adam optimizer operates on the pseudogradient as is also done by Kunin et al. [2020]). Each base learning rate is linearly warmed up to its corresponding value for 6 epochs followed by 90% decay at 30, 60, and 80 epochs, training for 100 epochs total, as prescribed by Buchlovsky et al. [2019].

The AlexNet model function code can be found here: `https://github.com/neuroailab/lr-identify/blob/main/tensorflow/Models/alexnet.py`. The ResNet model function code for both variants can be found here: `https://github.com/neuroailab/lr-identify/blob/main/tensorflow/Models/resnet_model_google.py`.

A.2 SimCLR

The architectures trained on this task are the same as in §A.1, namely, AlexNet, AlexNet-LRN, ResNet-18, ResNet-18v2, ResNet-34, and ResNet-34v2. Following Chen et al. [2020], for all models we use the same ImageNet preprocessing with $224 \times 224 \times 3$ sized images, L2 regularization of 1×10^{-6}, and two contrastive layers after dropping the final ImageNet categorization layer of the model, adapting their implementation provided here: `https://github.com/google-research/simclr/`. The only difference is that given that our batch sizes are small (between 128-512), we do not use the LARS optimizer [You et al., 2017] nor do we aggregate batch examples and batch norm statistics across TPU shards, in order to keep the learning rule and model architectures comparable across the other datasets. The learning rule hyperparameters are otherwise the same as in §A.1.

The SimCLR model function code can be found here: `https://github.com/neuroailab/lr-identify/blob/main/tensorflow/Models/simclr_model.py`.

A.3 Word-Speaker-Noise (WSN)

This is the word recognition task described in Kell et al. [2018], but with an updated dataset from Feather et al. [2019] that consists of 793 word class labels (and a null class when there is no speech), with the inputs being cochleagrams generated from waveforms of speech segments (from the Wall Street Journal [Paul and Baker, 1992] and Spoken Wikipedia Corpora [Köhn et al., 2016]) that are superimposed on AudioSet [Gemmeke et al., 2017] background noises. There are 5,810,600 training cochleagrams and 369,864 test set cochleagrams, where

each cochleagram is of dimensions $203 \times 400 \times 1$. The architectures trained on this task are the same as in §A.1 (with the exception that their final readout layer consists of 794 output units as opposed to 1000 output units), namely, AlexNet, AlexNet-LRN, ResNet-18, ResNet-18v2, ResNet-34, and ResNet-34v2. The learning rule hyperparameters and L2 regularizations are otherwise the same as in §A.1.

The WSN model function code can be found here: `https://github.com/neuroailab/lr-identify/blob/main/tensorflow/Models/audionet_model.py`.

A.4 CIFAR-10

This dataset [Krizhevsky, 2010] consists of 50,000 training images and 10,000 test set images, all of which are of dimensions $32 \times 32 \times 3$. We applied standard CIFAR-10 data augmentations used by the Keras library of random height and width shift, followed by a random horizontal flip. The architectures trained on this task are KNet4, KNet4-LRN, KNet5, and KNet5-LRN. KNet4-LRN is due to Krizhevsky [2012], and the 5 layer variant KNet5 we use adds an extra convolution layer (5×5 kernel size with 128 output channels) with a ReLU followed by average pooling with a kernel size of 3×3 and a stride of 2×2. The models use an L2 regularization of 1×10^{-5} for all learning rules, except for IA which used an L2 regularization of 1×10^{-12} (L2 regularization in IA is an important metaparameter for its learning stability).

The base learning rate for SGDM and IA is set to 0.01 for a batch size of 256, and linearly rescaled for the remaining batch sizes. For FA and Adam across all models, this base learning rate is 0.001. Unlike the other datasets, we found the best top-1 performance by setting the base learning rate to be constant for the entire 100 epochs of training with no learning rate warmup.

The KNet model function code can be found here: `https://github.com/neuroailab/lr-identify/blob/main/tensorflow/Models/knet.py`.

B Classifier Training Details

B.1 Feature Selection Procedure

As there are 1,056 training experiments across all learning rules, each model is trained for 100 epochs on its own Tensor Processing Unit (TPUv2-8 and TPUv3-8), saving checkpoints every 5 epochs, resulting in 21 samples in a single trajectory. Once all the models are trained, we generate on GPU their observable statistics (per layer) from their saved checkpoints, on the respective dataset's validation set (averaged across all validation stimuli). The resultant dataset of generated observables therefore consists of 20,736 total examples. For each example, an observable statistic is *not* used if and only if it had a divergent value during the course of training for any task, architecture, or learning rule hyperparameter, since all network parameters and units (as well as loss function and, when applicable, categorization performance) were well defined across these. Since each example in this resultant dataset is the concatenation of each observable statistic's trajectory, this corresponds to a total of at most 504 feature dimensions.

We additionally include the ternary indicator layer position ("early", "middle", or "deep"), determined by which third of the total number of layers for a given model each of its layers belongs to. For SimCLR, the two contrastive head layers are always assigned to "deep". This mapping for each model can be found in the `group_layers()` function defined here: `https://github.com/neuroailab/lr-identify/blob/main/tensorflow/Models/model_layer_names.py`.

B.2 Parameter Selection Procedure

We run all classifiers on ten category-balanced train/test splits, which are always (with the exception of architecture, learning curriculum, and task holdouts in Figs. 2(b), S3, S4) 75%/25% in proportion. For each train/test split, we perform five-fold stratified cross-validation for each classifier's parameters. The SVM and Random Forest use `scikit-learn` 0.20.4.

For the SVM, we use the `svm.LinearSVC` function in `scikit-learn`. PCA can be applied to the trajectories of the continuous valued observables as a preprocessing step (namely, excluding the ternary feature of layer position), and the binary decision to use it is chosen at the cross-validation stage. Specifically, when PCA is applied, the number of components $\in \{10, 20, 30, 40, 50, 100, 200, 300, 400, 500, 600\}$. The strength of the regularization parameter $C \in \{1.0, 50, 500, 5 \times 10^3, 5 \times 10^4, 5 \times 10^5, 5 \times 10^6\}$.

For the Random Forest, we use the `ensemble.RandomForestClassifier` function in `scikit-learn`. We allow for the number of trees in each forest to be $\in \{20, 50, 100, 500, 1000\}$. We allow the number of features to consider at each split of an internal node to be $\in \{n_{feats}, \log_2(n_{feats}), \sqrt{n_{feats}}\}$, where n_{feats} is the total number of input features.

For the Conv1D MLP, we use TensorFlow 1.13.1 to train a two-layer neural network that consists of a learned 1-layer 1D convolution, followed by a ReLU and (optional) pooling prior to the fully connected categorization layer. We use the Adam optimizer [Kingma and Ba, 2014] to train the classifier on a separate Titan X GPU per split for 400 epochs. The Adam learning rate is set to be $\in \{1 \times 10^{-3}, 1 \times 10^{-4}\}$. The train batch size is set to be $\in \{512, 1024\}$. The kernel size of the 1D convolution is set to be a fraction of the trajectory length $\in \{3 \times 10^{-3}, 7 \times 10^{-3}, 5 \times 10^{-2}, 0.25, 0.5, 1.0\}$. The strides of the 1D convolution is set to be $\in \{1, 2, 4\}$. The number of output filters of the 1D convolution is set to be $\in \{20, 40\}$. The binary choice of a pooling layer between the 1D convolution and fully connected categorization layer is chosen during cross-validation and if used, can be either 1D max pooling or 1D average pooling. L2 regularization is set to be $\in \{1 \times 10^{-4}, 0\}$.

The classifier code can be found in: `https://github.com/neuroailab/lr-identify/blob/main/fit_pipeline.py`. The classifier cross-validation parameter ranges can be found in: `https://github.com/neuroailab/lr-identify/blob/main/cls_cv_params.py`.

B.3 Variability of Generalization

The second aim of this study is to understand whether the approach described above generalizes to selected variations in the available data. We introduce two variations: (1) **trajectory subsampling**, in which data is taken for part of the model learning trajectory, and (2) **holdouts**, in which all but one "animals", "curricula", and "tasks" are used only during training and the remaining one is used only during testing. (1) investigates whether our discriminative approach is successful when only part of the model training process is available, and (2) investigates where it transfers successfully to unseen classes of input types. These two variations address the fact that neural and behavioral data is usually *not* collected throughout the developmental trajectory of the animal's entire lifespan as well as generalization (particularly) to new animals and curricula.

B.3.1 Trajectory Subsampling

Trajectory subsampling is performed to represent data taken at a low frequency, data taken for short periods of time, and data taken at different points in the training process. All of these are defined relative to our "full" model learning trajectory, which is generated from epochs $E = \{0, 5, 10, \ldots, 95, 100\}$ spanning the entire 100 epochs, where $|E| = 21$ samples since we sample every 5 epochs during model training. We note that this is inherently subsampled, but we find that it is a good proxy for the entire model learning trajectory while avoiding the prohibitive computational complexity of generating observable statistics for each step across the 100 epochs of every model training process.

We therefore consider a subsampled dataset to be generated from epochs $E' \subset E$. We define three quantities to represent this limitation. **Subsample start position** is the epoch in the model learning trajectory from which the subsampled dataset starts. **Subsample period** is the space between two consecutive samples of the learning trajectory (in units of model training epochs). We consider three subsample periods of 5 epochs (the original value), 15 epochs, and 25 epochs, which correspond to "Dense Subsampling", "Intermediate Subsampling", and "Sparse Subsampling" in Fig. 4(a), respectively. Finally, **subsample proportion** is the proportion of the number of samples chosen for the trajectory subsample relative to that of the overall model learning trajectory (21 total samples). In Fig. 4(a), we represent this as a percentage of the total trajectory, but the number of samples this corresponds to in the "Dense Subsampling" regime is 2, 4, 6, 9, 11, 13, 16, 18, and 21 samples (the latter is the full trajectory); in the "Intermediate Subsampling" regime it is 2, 4, and 6 samples; and in the "Sparse Subsampling" regime it is 2 and 4 samples. We use a different *single* random seed (corresponding to a potentially different subsample start position) for each example to keep the size of the dataset the same (in terms of number of examples) as when the full model learning trajectory is present.

B.3.2 Holdouts

We hold out certain parts of the dataset from training and use them for testing to understand the transfer capability of a classifier that can separate certain learning rules when encountering new learning rules. We start by considering two types of holdouts: **animals** and **curricula**. We consider an "animal" to be a certain architecture (one of ten) and a "curriculum" to be a certain combination of batch size and dataset randomization seed (one of six), and hold them out by using the remaining animals or curricula in the classifier training set and the held-out one in the classifier testing set. Specifically, for each of the ten architectures, we train the classifier on the data for the other nine architectures and test on the remaining one. We do the same for the six batch size/dataset randomization seed combinations. We also consider **task** holdouts to get a sense of the differences in learning dynamics across different tasks, holding out all examples from each one of the four tasks. We then measure the test accuracy for each holdout.

B.4 Realistic Data Measurements: Unit Subsampling and Noise Robustness

Thus far we have assumed that whenever data is collected, it can be collected perfectly: no noise, no loss of neurons. In the final aim of this study, we address how our approach handles more realistic situations under which neuroscience data is collected, we analyze the noise robustness and sample efficiency of the observable statistics. We consider the ResNet-18 architecture trained on supervised ImageNet and self-supervised SimCLR with either the FA or IA learning rules, using a batch size of 256, model seed of None, and dataset randomization seed of None. For noise robustness, we add Gaussian noise ($\sigma = 0, 0.5, 1, 5, 10$) to the (forward) weight/activation/layer-wise activity change matrix of each layer before generating observable statistics. For sample efficiency, we randomly subsample the units from the matrix at rates of $3 \times 10^{-3}\%$, $2.08 \times 10^{-2}\%$, $1.44 \times 10^{-1}\%$, 1%, 10%, 25%, 50%, 75%, and 100%. We consider test accuracy for the Cartesian product of these two axes. For each Cartesian product, we use the *same* random seed for unit subsampling and Gaussian noise. The number of random seeds depends on the unit subsample fraction based on how many are needed until test performance stabilizes when averaged across random seeds and ten category-balanced 75%/25% train/test splits. Thus, smaller unit subsample fractions will require more random seeds (and are computationally more efficient to generate data from) than larger fractions, which will require fewer. Specifically, we use six random seeds for $3 \times 10^{-3}\%$, four random seeds each for $2.08 \times 10^{-2}\%$ and $1.44 \times 10^{-1}\%$, three random seeds for 1%, and two random seeds for each of the remaining unit subsample fractions.

C Supplementary Figures

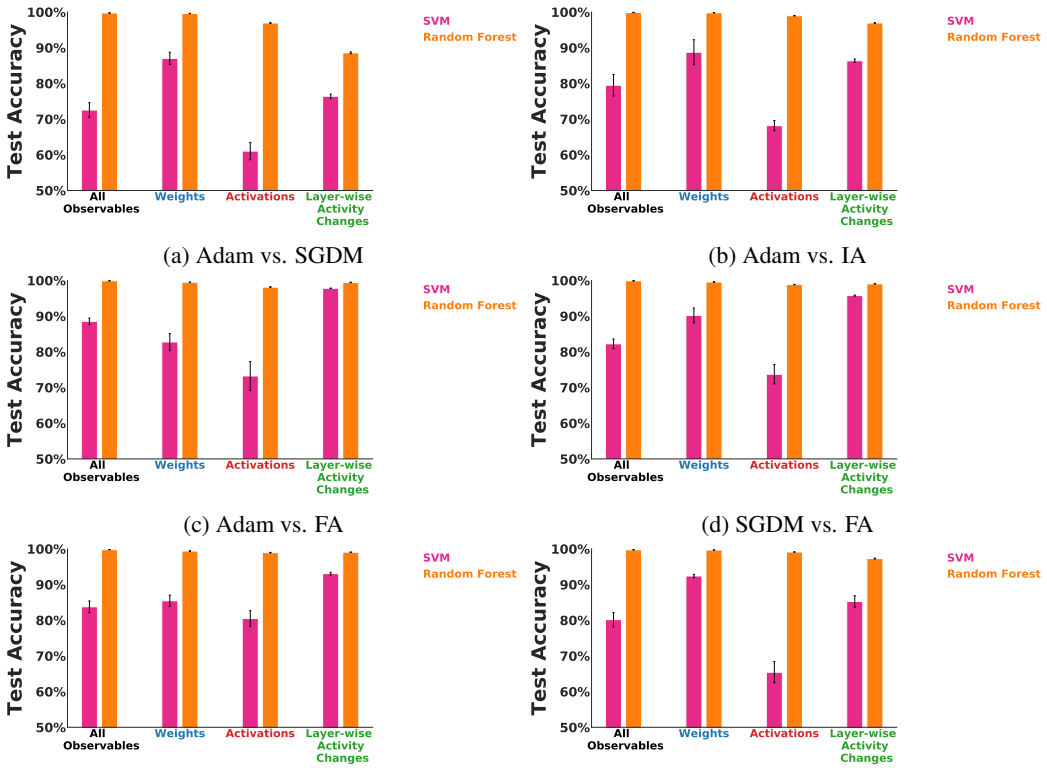

(a) Adam vs. SGDM

(b) Adam vs. IA

(c) Adam vs. FA

(d) SGDM vs. FA

(e) FA vs. IA

(f) SGDM vs. IA

Figure S1: **Learning rule is least able to be *linearly* determined from the activations for any pair of learning rules.** For all six pairs of learning rules, we train a separate classifier to distinguish each learning rule pair per observable measure. Mean and s.e.m. are across ten category-balanced 75%/25% train/test splits. Chance performance in these settings is 50% test accuracy.

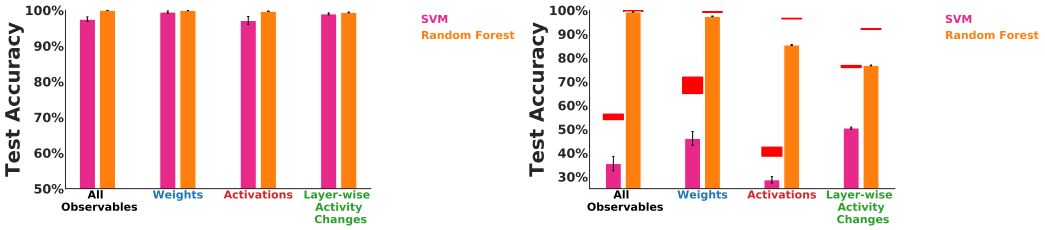

(a) Task performance as a confounded indicator of learning rule separability.

(b) Averaging across the trajectory can hurt generalization.

Figure S2: **Learning rule separability controls. (a)** We train classifiers to separate IA vs. SGDM when their top-1 validation accuracy is similar on ImageNet, namely across all learning hyperparameters for ResNet-18, ResNet-18v2, ResNet-34, and ResNet-34v2. Mean and s.e.m. are across ten category-balanced 75%/25% train/test splits. Chance performance in this setting is 50% test accuracy. **(b)** We train classifiers to separate all four learning rules after averaging the statistics across the trajectory. Red lines indicate test set performance of each classifier when trained on the entire trajectory for each respective observable measure, as reported in Fig. 2(a). Mean and s.e.m. are across ten category-balanced 75%/25% train/test splits. Chance performance in this setting is 25% test accuracy.

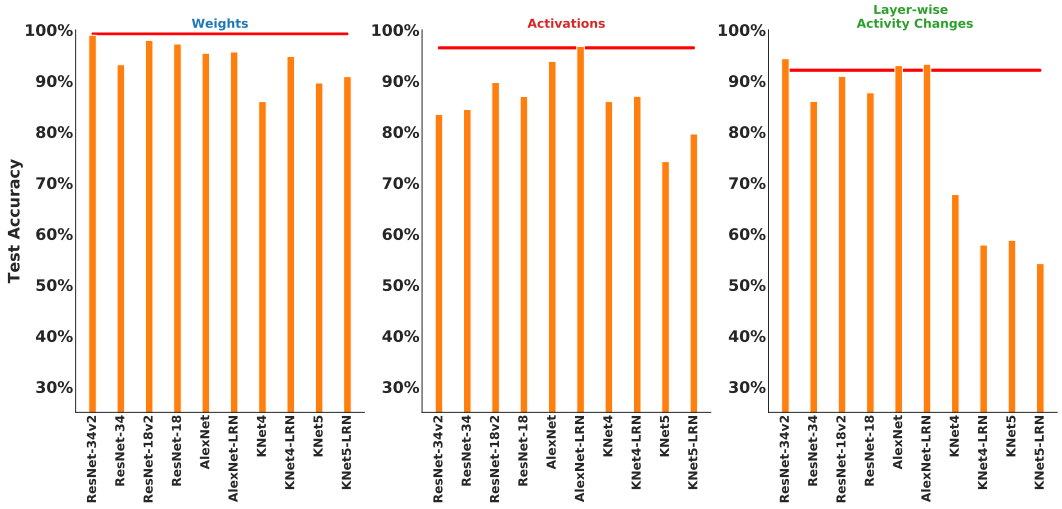

(a) Heldout architecture

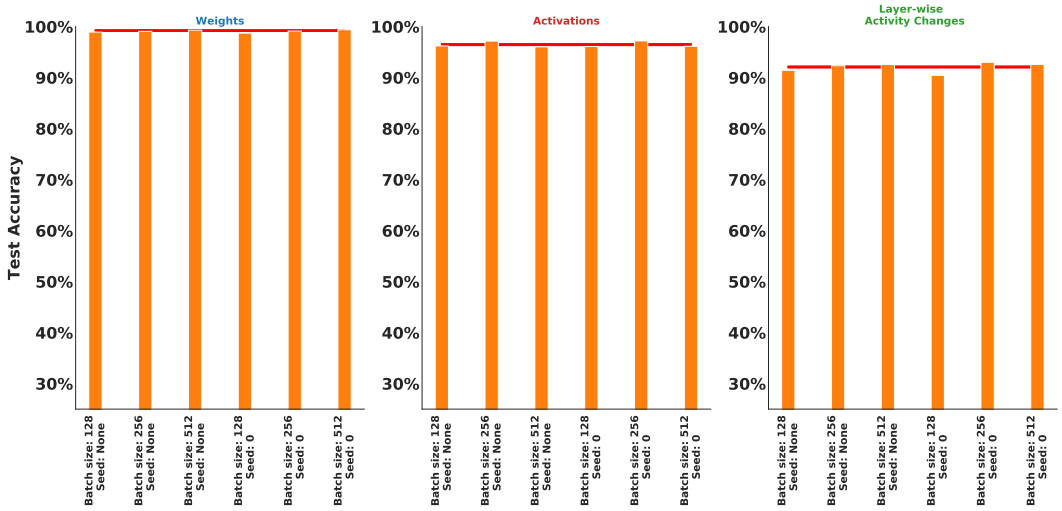

(b) Heldout training curriculum

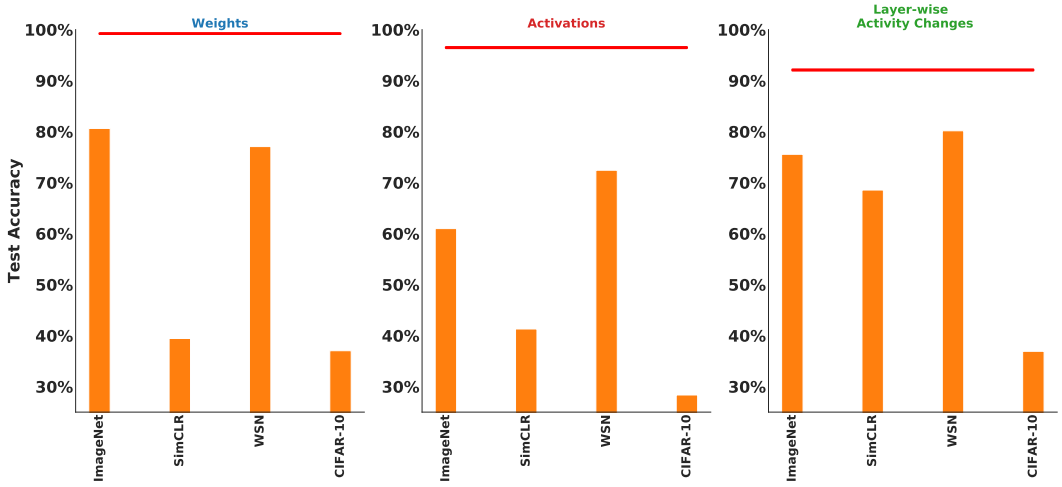

(c) Heldout task

Figure S3: **Assessing robustness of generalization for individual observable measures (Random Forest).** Let the red line indicate the mean and s.e.m. test accuracy from Fig. 2(a) for the Random Forest trained on each observable measure. **(a)** We hold out *all* examples from each of the ten architectures. **(b)** We hold out *all* examples from each of the six combinations of batch size and dataset randomization seed pair. **(c)** We hold out *all* examples from each of the four tasks. Chance performance is 25% test accuracy.

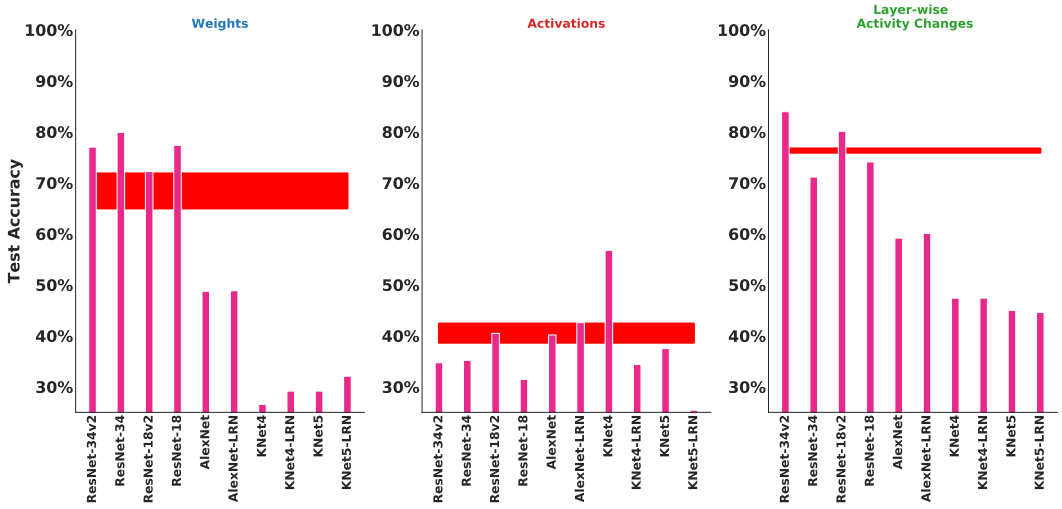

(a) Heldout architecture

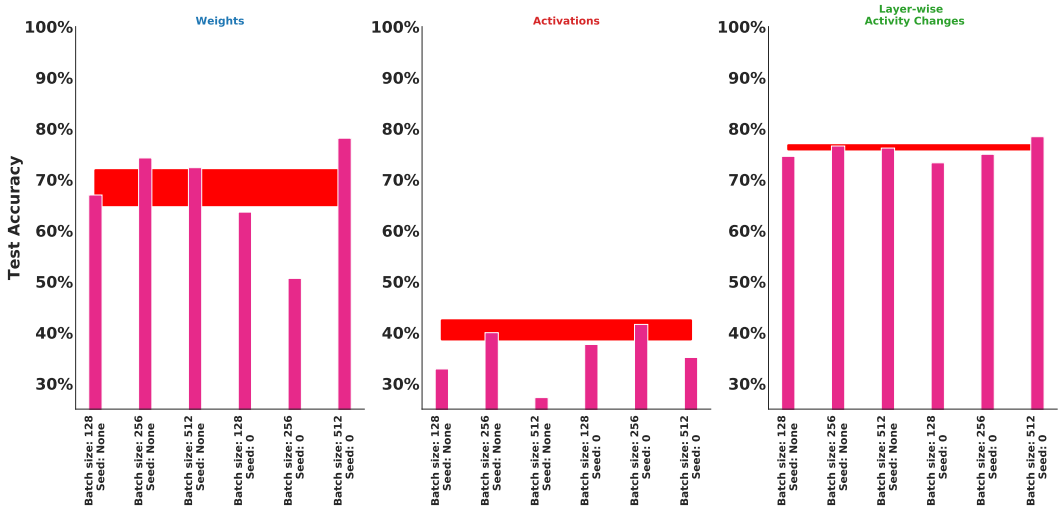

(b) Heldout training curriculum

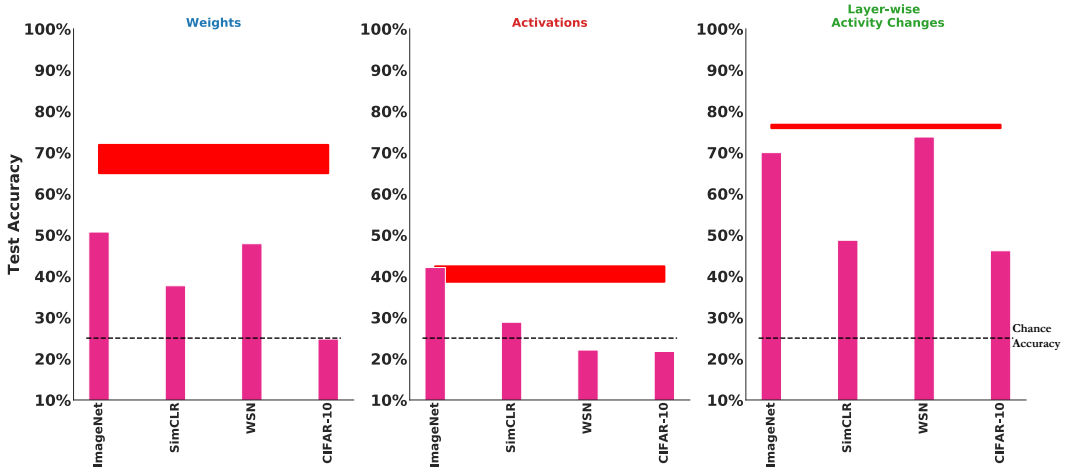

(c) Heldout task

Figure S4: **Assessing robustness of generalization for individual observable measures (SVM).** Let the red line indicate the mean and s.e.m. test accuracy from Fig. 2(a) for the SVM trained on each observable measure. **(a)** We hold out *all* examples from each of the ten architectures. **(b)** We hold out *all* examples from each of the six combinations of batch size and dataset randomization seed pair. **(c)** We hold out *all* examples from each of the four tasks. Chance performance is 25% test accuracy.

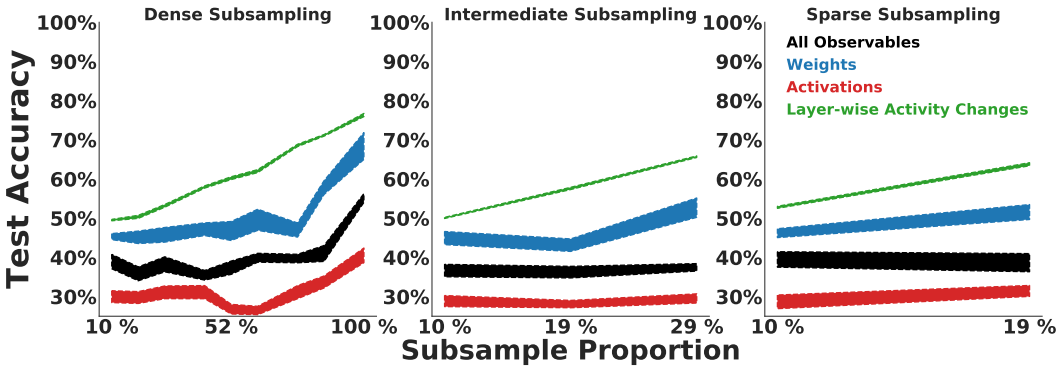

Figure S5: **Sparse subsampling *across* the learning trajectory is robust to trajectory undersampling (SVM).** For each observable measure, the test accuracy of the SVM on a random 25% split of the data. Mean and s.e.m. are across the ten category-balanced 75%/25% train/test splits. Each"full" training trajectory contains 21 samples (corresponding to epochs $0, 5, 10, \cdots, 100$). "Subsample Proportion $Y\%$" refers to the number of samples chosen for the trajectory subsample relative to that of the full trajectory (21 total samples). Chance performance in these settings is 25% test accuracy.

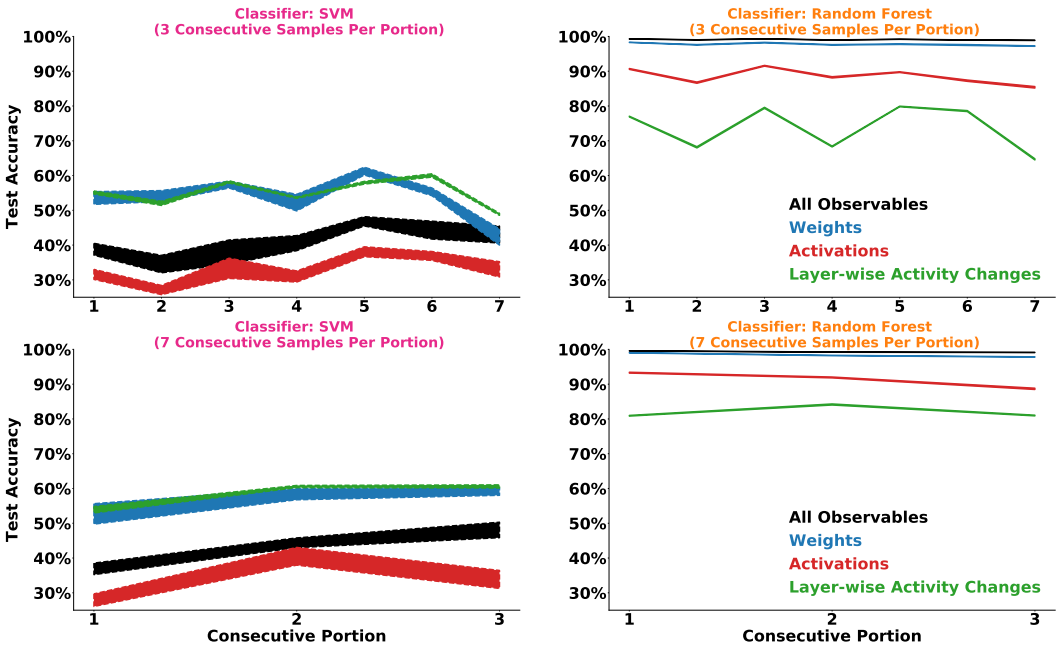

Figure S6: **Generalization performance can vary when trained solely on a consecutive portion of the learning trajectory, regardless of classifier.** For each observable measure, the test accuracy on a random 25% split of the data. Mean and s.e.m. are across the ten category-balanced 75%/25% train/test splits. Each training sample contains each consecutive seventh of the trajectory, totalling 7 consecutive portions each consisting of 3 samples (top row), or consecutive third of the trajectory, totalling 3 consecutive portions each consisting of 7 samples (bottom row). Chance performance in these settings is 25% test accuracy.

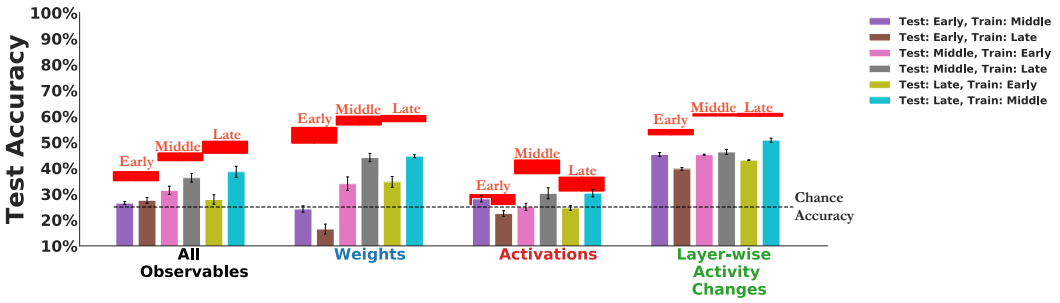

Figure S7: **Training solely on consecutive portions of the learning trajectory is *not* robust to trajectory undersampling (SVM).** We train the SVM on 75% of examples with access to only one consecutive third of the full trajectory (7 consecutive samples each out of 21 total samples), testing on the remaining 25% of examples from one of the other two consecutive thirds. Red lines denote SVM performance when tested on 25% of examples from the *same* portion of the trajectory as in classifier training for each observable measure, reported in the bottom left row of Fig. S6. Mean and s.e.m. in all cases are across ten category-balanced train/test splits. Chance performance in this setting is 25% test accuracy (denoted by the dotted black line).

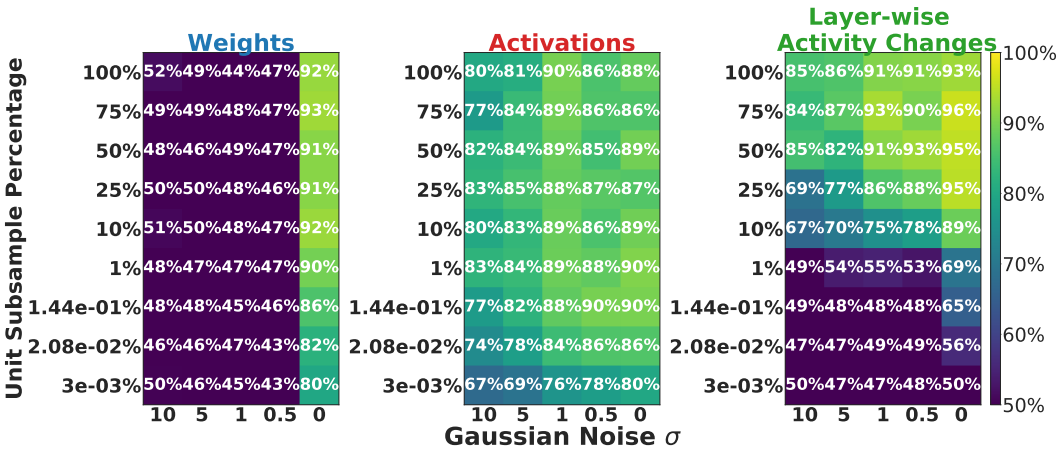

Figure S8: **Activations are the most robust to measurement noise and unit undersampling (SVM).** For each observable measure, the SVM test accuracy separating FA vs. IA on ResNet-18 across the ImageNet and SimCLR tasks, averaged across random seed and ten category-balanced 75%/25% train/test splits. The x-axis from the left to right of each heatmap corresponds to decreasing levels of noise, and the y-axis from bottom to top corresponds to increasing levels of sampled units. Top right corner of each heatmap corresponds to the perfect information setting of §4. Chance performance in this setting is 50% test accuracy.